Extreme Mechanics Letters 39 (2020) 100824

Contents lists available at ScienceDirect

Extreme Mechanics Letters

journal homepage: www.elsevier.com/locate/eml

Self-adaptive flexible valve as passive flow regulator

Qiang Zhang [a,b], Xirui Peng [a], Shayuan Weng [a,c], Rundong Zhang [d], Daining Fang [b,e], Ruike Zhao [d], H. Jerry Qi [a,*]

[a] The George W. Woodruff School of Mechanical Engineering, Georgia Institute of Technology, Atlanta, GA 30332, USA
[b] State Key Laboratory for Turbulence and Complex System, College of Engineering, Peking University, Beijing, 100871, People's Republic of China
[c] College of Aerospace Engineering, Chongqing University, Chongqing, 400044, People's Republic of China
[d] Department of Mechanical and Aerospace Engineering, The Ohio State University, Columbus, OH 43210, USA
[e] Institute of Advanced Structure Technology, Beijing Institute of Technology, Beijing, 100081, People's Republic of China

ARTICLE INFO

Article history:
Received 21 April 2020
Received in revised form 23 May 2020
Accepted 5 June 2020
Available online 9 June 2020

Keywords:
Self-adaptive valve
Passive valve
Flow regulator
Fluid–structure interaction
3D printing

ABSTRACT

Valves are widely used in fluidic channel systems to regulate flows. In many applications, maintaining a constant flow rate under varying input conditions is critical. However, current active or passive valves suffer from several drawbacks, such as complex structures, complicated fabrication processes, and complex operational procedures. This paper presents a novel design concept for fluidic channels using a simple structure that can serve as self-adaptive passive valves to regulate flow under external pressure. The design relies on embedding a cantilever-like flap inside a channel to provide a self-regulated closed-loop control of the flow. The flap can passively deform to adapt to the variation of the fluid pressure. A theoretical model is developed and validated by finite-element simulations to understand the flow characteristics of this design. Based on the theoretical model, we provide the design rules for obtaining valves with desired pressure-flow rate responses. Furthermore, by integrating the quantitative design tool and 3D printing, a valve that can maintain a constant flow rate over a certain pressure range is designed, fabricated, and characterized. With support from systematic analysis and rapid manufacturing techniques, the valve design proposed here can open routes for applications in microfluidic systems and drug infusion systems.

1. Introduction

The last two decades have witnessed the rapid development of microfluidic systems and its broad applications, such as biomedical devices [1], analytical systems [2], and tools for chemistry and biochemistry [3]. In many of these applications, precision control of flow rate is essential (Fig. 1a). For example, in a flow chemistry system, the ratio of reagents' flow rate needs to be accurately controlled because it defines the reaction stoichiometry and changing the flow rate affects the final reaction products [4,5]. In a drug infusion or microdialysis system [6,7], overdose, which may be caused by an uncontrolled delivery rate, can be even life-threatening (i.e., coma or death). Currently, in order to control the flow rate, one has to use pumps or valves that can compensate for the changes in external conditions, such as pressure. The traditional valves for flow control require sophisticated external electronic/mechanical devices to provide a closed-loop control [8]. For example, an insulin pump is a highly integrated device composed of a glucose measuring module and a pumping system to dispense insulin in a controlled rate and volume to patients with type-I diabetes [9,10]. By detecting the glucose level in a human body through the glucose measuring module and then transmitting the data to the insulin pump [11], the insulin pump provides the required basal insulin, a background insulin with a constant flow rate over a period of fasting, to keep blood glucose levels at consistent levels. In a closed-loop control system of pumps, flow-regulating valves are usually designed by integrating active movable components such as a diaphragm-like structure that can be actuated by piezoelectric [12,13], pneumatic [14–17], electrostatic [18,19], light [20] or magnetic forces [21,22]. When there is a pressure change, sensors detect the change and send the information to a central processor, which calculates the changes and controls the valve to respond. The valves in these systems are called active valves. Although active valves respond rapidly and have accurate control of the flow, they have drawbacks such as the requirement of many sensors, processors, actuators, and software to work collaboratively, which increases the control complexity, failure risk, and maintenance cost.

Alternatively, passive valves that respond to pressure changes and operate adaptively without the assistance for external devices could significantly simplify the valve structure and operation [25–28]. An excellent example of the passive valves is the

* Corresponding author.
E-mail address: qih@me.gatech.edu (H.J. Qi).

https://doi.org/10.1016/j.eml.2020.100824
2352-4316/

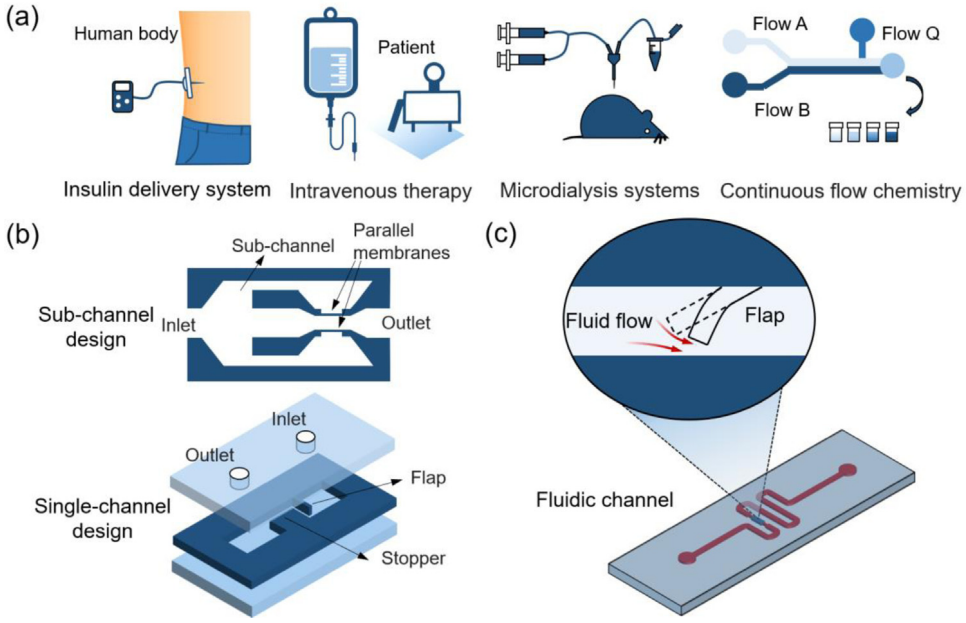

Fig. 1. Designs for the passive valves and their potential applications. (a) Applications in the biomedical and chemistry areas that require the flow rate to be accurately controlled. (b) Existing passive valve designs that utilize sub-channels (top panel, reproduced from Fig. 1 from Ref. [23]) or a single channel (bottom panel, reproduced from Fig. 3 from Ref. [24]). (c) Schematic graph of the design for the self-adaptive flexible valve as a passive flow regulator.

heart valve, which opens and closes passively due to the pressure difference across the valve [29]. With the passive response, these valves allow the possibility for a closed-loop control over the flow without complicated sensors and computing algorithms. Currently, most of the passive valves rely on creating a structure that includes a sub-channel (serving as the control channel) to regulate flow. For example, Doh et al. [23] demonstrated a passive flow regulator relying on using two sub-channels to control the autonomous deflection of parallel membrane valves (the top panel in Fig. 1b). There are also works utilizing a single channel, while it lacks flexibility and has few degrees of freedom to be designed. For example, Yang et al. used a self-adaptable check-valve to obtain a stable flow rate under a range of pressure change (70–200 kPa; the bottom panel in Fig. 1b) [24,30]. In their design, three edges of the flap are clamped so that the flap-stopper contacting area and the flow resistance can passively respond to pressure changes via the bulging deformation of the flap. Despite these progresses, the existing passive valve designs still suffer from some limitations, such as the requirement of complicated structures and fabrication process. For example, the sub-channel design, which is the most popular type, requires multiple channels to be arranged in different spatial locations, leading to complicated procedures to fabricate [31–33]. Additionally, careful studies on the nonlinear flow rate-pressure relationship, which are important in determining design parameters in these designs, are very limited. Very recently, Xiang et al. developed a new flow regulator with a very simple structure and a high throughput up to several milliliters per minute. By embedding a suspended elastic membrane with a hole into the flow channel, the regulator they developed is able to stabilize the flow rate under a low threshold pressure [34].

In this paper, we present a simple yet efficient design of a fluid channel that can act as a passive valve to maintain a constant flow rate over a certain range of pressure. The key concept is to embed a cantilever-beam like flexible flap as a valve into a long, narrow channel (Fig. 1c). The design presented here allows the quantitative selection of the relevant structural parameters for accurately tuning the nonlinear flow rate-pressure relation. Different from the existing designs, our design uses single flow channel and leverages the flap bending to self-adaptively respond to the pressure change, thereby enabling a rather simple structure but with a highly tunable response. In order to understand the flow characteristics of this design, we also develop a theoretical model for the nonlinear flow rate-pressure relationship that incorporates the relevant design parameters of the flap. To validate the model, a finite-element analysis (FEA) that considers the fluid–structure interaction is performed. Based on the model, we provide the design guidelines for the valves with optimized flow-regulating performance. Following the guidelines, we select a specific design as an example for fabricating a valve that can provide an almost constant flow over the pressure range of 20–60 kPa. According to requirements, other design points that alter material and geometric properties can also be chosen for obtaining a different pressure change. We anticipate that our new valve design can be useful for potential applications such as chemical reactions, microfluidic sorting, and portable drug infusion systems.

2. Design, analysis, and methods

2.1. Structure and design principle

The inset in Fig. 2a schematically shows the cross-section of the valve in our design. To provide a closed-loop control of the flow, a tilted deformable flap (dashed line in Fig. 2a) is fixed to the inner ceiling of the channel, serving as a flow regulator. When the flow rate is higher than the targeted value, a higher pressure is applied to the flap, which bends the flap toward the bottom wall of the channel (the deformed configuration; solid line in Fig. 2a) and reduces the gap between the flap tip and the bottom wall to lower the resultant flow rate. And vice versa. In this way, the flow rate within the channel can be regulated by the flap via its passive deformation under the changing pressure. The dimension and the material property of the flap affect its bending behavior and thus the flow-regulation performance. In this work, we use the same material for the flap and investigate how the flap's geometrical parameters affect the flow-regulation performance. Three critical geometry parameters are studied, including the flap thickness t, the tilt angle of the flap relative to the top wall θ, and the initial gap between the flap tip and the bottom wall d_0 (Fig. 2b).

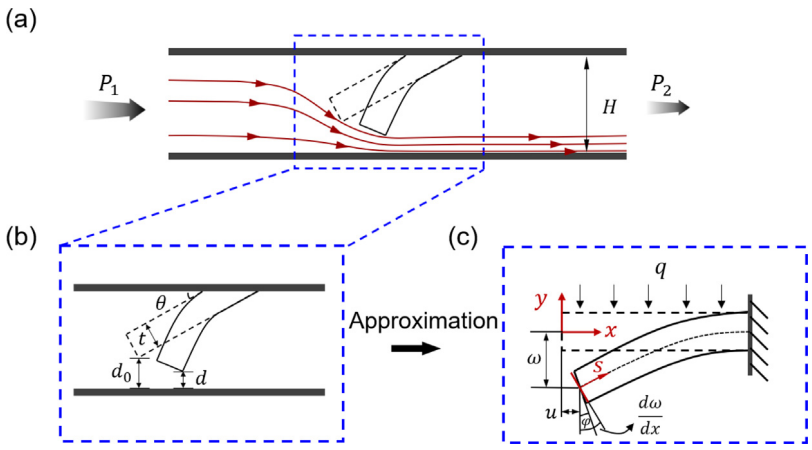

Fig. 2. Schematic diagrams of the valve design for passive flow regulating. (a) Schematic graph of the fluid flow and deformation of the flap within a channel (height, H) under a pressure difference ($P_1 - P_2$). (b) Schematic graph of the details of the flap deformation. The flap with a tilt angle of θ and flap thickness of t changes from its initial configuration (dashed line) to a new position (solid line), during which the gap changes from d_0 to d. (c) Schematic graph of the deformation of a Timoshenko cantilever beam under a uniformly distributed load q. This can be used as a rational approximation of the flap deformation induced by the fluid pressure in Fig. 2b. The local coordinate (s) along the neutral axis of the beam and the Cartesian coordinate o-xy are denoted in the figure, respectively.

2.2. Theoretical analysis

To gain insight into the physics behind the different regulation behaviors governed by the design parameters, t, θ, and d_0, we theoretically analyze the deformation of the flap and its influence on the flow rate-pressure relation. As shown in Fig. 2a–b, we consider a two-dimensional fluidic channel (of height H) with a flap, which has a thickness t, tilt angle θ, and initial gap d_0. At the initial moment, the channel is filled with a working fluid and the flap is in its initial undeformed configuration. The fluid starts to flow due to a pressure difference ΔP ($\Delta P = P_1 - P_2$) across the channel. The top and bottom channel walls are considered to be rigid. As the flap is soft, it deforms under the flow-induced pressure. Its deformation is determined by the magnitude of the pressure acting on it, which further contributes to the flow rate control. We consider that after a series of quasi-static equilibrium processes as the pressure difference gradually increases from 0 to ΔP, the flap eventually transforms from the initial undeformed configuration (dashed line) into a new deformed configuration (solid line) and the gap between the flap tip and the bottom wall has a new value d (Fig. 2b). In order to quantitatively describe the flap deformation and calculate d, we consider the flap as a straight cantilever (Fig. 2b vs. c). Hence, the length of the beam l is determined by the distance from the flap tip on the top surface to its root, which can be written as

$$l = (H - d_0 - t\cos\theta)/\sin\theta \tag{1}$$

Here, we consider a relatively thick beam, i.e. $l/t < 5$. Moreover, considering that the boundary layer is very thin and the pressure is nearly homogeneous across the cross section, the pressure difference ΔP that the surrounding fluid applies on the flap can be approximately represented as a uniformly distributed load q applying on the beam surface through the relation $q = \Delta P W_{flap}$, where W_{flap} is the width of the flap (Fig. 2c). It should be noted that large beam deflection under high pressure would cause nonlinear behavior of the beam, which affects the approximation using our model. To include the nonlinearities caused by the finite rotation of the flap, and note that the length-thickness ratio of the flap is relatively small, we employ the nonlinear Timoshenko beam theory to calculate the beam deformation. Following the schematic graph of the beam deformation in Fig. 2c, when subjected to a distributed load q, the thick beam deforms from the reference configuration (dashed line) into the current configuration (solid line). Using the Lagrangian description, the kinematic relations during deformation can be expressed as [35]

$$u_x(x, y) = u - y\sin\varphi \tag{2a}$$

$$u_y(x, y) = \omega(x) - y(1 - \cos\varphi) \tag{2b}$$

where u_x and u_y denote the displacement components at an arbitrary position in the beam in the x- and y-axis directions, respectively. u and ω are the displacement components at the neutral axis in the x- and y-directions, respectively. φ represents the rotational angle of the normal to the mid-surface of the beam. If φ is restricted to small values, then $\sin\varphi \approx \varphi$ and $1-\cos\varphi \approx 0$, and Eq. (2) recovers to the classical linear Timoshenko theory. It should be mentioned that although the rotation here can be large, the strains in the flap are still in the small-strain range. Therefore, the length of the neutral layer of the beam does not change and still holds for l. From the strain–displacement relations for small strains, the non-zero strains based on the Timoshenko assumptions are [35]

$$\varepsilon_{xx} = \frac{\partial u_x}{\partial x} = -y\frac{\partial \sin\varphi}{\partial x} \tag{3a}$$

$$\varepsilon_{xy} = \frac{1}{2}\left(\frac{\partial u_x}{\partial y} + \frac{\partial u_y}{\partial x}\right) = \frac{1}{2}\left(-\sin\varphi + \frac{\partial \omega}{\partial x}\right) \tag{3b}$$

The expressions for the bending moment M_z and shear force Q_y in the beam can be written as follows [35]

$$M_z = \int y\sigma_{xx}dA = \int yE\varepsilon_{xx}dA = -EI\cos\varphi\frac{d\varphi}{dx} \tag{4a}$$

$$Q_y = \kappa\int \sigma_{xy}dA = \kappa\int 2G\varepsilon_{xy}dA = \kappa AG\left(-\sin\varphi + \frac{d\omega}{dx}\right) \tag{4b}$$

where E is the elastic modulus, I is the moment inertia of the cross-sectional area, κ is the Timoshenko shear coefficient, A is the cross-section area, G is the shear modulus, respectively. For the convenience of describing the large deflection of the beam, we also need to describe the bending moment and shear force in the local coordinate s that is along the neutral axis of the beam in the deformed configuration (Fig. 2c). In the local coordinate s, the shear force on a surface that is perpendicular to the neutral axis can be expressed as$Q_{\perp s} = qs\cos\alpha$ (where α is the rotation angle of the plane tangent to the mid-surface), while the shear force in a surface that is along the y-axis direction is $Q_y = qs$. The equilibrium equation in the deformed configuration requires that

$dM_z/ds = Q_{\perp s}$. With these relations, Eq. (4) can be rewritten as

$$-EI\frac{d}{ds}\left(\cos\varphi\frac{d\varphi}{dx}\right) = qs\cos\alpha \tag{5a}$$

$$qs = \kappa AG\left(-\sin\varphi + \frac{d\omega}{dx}\right) \tag{5b}$$

Eq. (5) involves both the coordinate o-xy in the undeformed configuration and the local coordinate s in the deformed configuration. The two coordinate systems satisfy the relationship

$$\frac{dx}{ds} = \cos\alpha \tag{6a}$$

$$\frac{dy}{ds} = \sin\alpha \tag{6b}$$

where α obeys the following relation

$$\tan\alpha = \frac{d\omega}{dx} \tag{6c}$$

It should be noted that $d\omega/dx \neq \varphi$ due to the shear effects considered in the Timoshenko beam hypothesis. Inserting Eq. (6) into Eq. (5) and use the trigonometric operations, we arrive at

$$\frac{d^2\varphi}{ds^2} = -\frac{qs}{EI\cos\varphi\left(1+\left(\frac{qs}{\kappa AG}+\sin\varphi\right)^2\right)} \tag{7a}$$

$$\frac{d\omega}{ds} = \frac{qs}{\kappa AG\sqrt{\left(1+\left(\frac{qs}{\kappa AG}+\sin\varphi\right)^2\right)}} + \frac{\sin\varphi}{\sqrt{\left(1+\left(\frac{qs}{\kappa AG}+\sin\varphi\right)^2\right)}} \tag{7b}$$

More details for deriving the above two equations can be found in the Supporting Information.

The above two equations constitute the governing equations for the large deformation problem of the beam under the distributed load q. The boundary conditions for this problem are $\varphi'(s=0) = 0$, $\varphi(s=l) = 0$, and $\omega(s=l) = 0$. After solving the equations, the deflection of the flap tip (bottom-right corner of the flap in Fig. 2b) ω_{tip}, the rotation angle of the flap end φ_{tip}, and the horizontal displacement of the center point at the flap end u_{tip}, for different levels of pressure can be obtained. To further calculate the new gap d in the deformed configuration, it is feasible to use the geometry relations that relate the bending flap to the initial straight one to express d in the function of ω_{tip}, φ_{tip}, and u_{tip}. This is expressed as

$$d = d_0 - \cos\left(\theta + \tan^{-1}\left(\frac{u_{tip}+\frac{t}{2}\sin\varphi_{tip}}{\omega_{tip}+\frac{t}{2}\cos\varphi_{tip}-\frac{t}{2}}\right)\right)\times \sqrt{\left(u_{tip}+\frac{t}{2}\sin\varphi_{tip}\right)^2+\left(\omega_{tip}+\frac{t}{2}\cos\varphi_{tip}-\frac{t}{2}\right)^2} \tag{8}$$

More details for deriving the above equation can be found in the Supporting Information. Eq. (8) can be further normalized by dividing H on both sides, which is expressed as

$$\frac{d}{H} = \frac{d_0}{H} - \cos\left(\theta + \tan^{-1}\left(\frac{\frac{u_{tip}}{H}+\frac{t}{2H}\sin\varphi_{tip}}{\frac{\omega_{tip}}{H}+\frac{t}{2H}\cos\varphi_{tip}-\frac{t}{2H}}\right)\right)\times \sqrt{\left(\frac{u_{tip}}{H}+\frac{t}{2H}\sin\varphi_{tip}\right)^2+\left(\frac{\omega_{tip}}{H}+\frac{t}{2H}\cos\varphi_{tip}-\frac{t}{2H}\right)^2} \tag{9}$$

After obtaining d for different levels of pressure, we couple it with the flow rate. Here, we avoid using Navier-Stokes equations to calculate the accurate velocity distribution inside the channel as it would involve complex computation due to the fluid–structure interaction. We make some simplifications so that an approximate relationship can be derived theoretically. We first consider the inviscid flow. After obtaining the volume flow rate for the inviscid flow, we can then add a constant which we refer to as the viscous correction coefficient (η) to obtain the flow rate for the actual viscous fluid. η is used to lump the influence of the viscosity on the final flow rate. Following the above discussion, we first seek to obtain the flow rate for the inviscid flow within the channel. Under this condition, the pressure drop across the channel before the flap is zero due to no cross-section change, and the velocity of the fluid for that part is homogeneous which can be denoted as v_1. This is also applicable to the fluid after the flap where the velocity is denoted as v_2. The pressure gradient across the channel now equals the pressure difference across the fluid flowing through the flap. In Fig. 2a, from left to right, we can apply the Bernoulli's equation along a streamline [36]

$$\frac{1}{2}\rho v_1^2 + P_1 = \frac{1}{2}\rho v_2^2 + P_2 \tag{10}$$

where v_1, P_1 is the velocity and pressure of the fluid on the left of the flap, v_2, P_2 is the velocity and pressure of the fluid on the right of the flap, respectively. The gravitational contribution to the total potential energy is negligible and does not appear in Eq. (10). Due to the conservation of mass, we have the relation as follows [36]

$$Q = A_1 v_1 = A_2 v_2 \tag{11}$$

where A_1 and A_2 are the cross-sectional areas of the fluid in the left and right of the flap, respectively. Considering a channel with a width of W, substitute HW for A_1 and dW for A_2, Eq. (11) can be written as

$$Q = HWv_1 = dWv_2 \tag{12}$$

Inserting Eq. (12) into Eq. (10) and compensating the flow rate loss due to fluid viscosity, we arrive at

$$Q = \eta HW\sqrt{\frac{2\Delta P}{\rho\left(\left(\frac{d}{H}\right)^{-2}-1\right)}} \tag{13}$$

where η can be determined by fitting the FEA simulations. By introducing the dimensionless flow rate $\overline{Q} = Q/\left(HW\sqrt{E/\rho}\right)$ and the dimensionless pressure difference $\overline{P} = \Delta P/E$, Eq. (13) can be rewritten as

$$\overline{Q} = \eta\sqrt{\frac{2\overline{P}}{\left(\left(\frac{d}{H}\right)^{-2}-1\right)}} \tag{14}$$

Through the analysis above, we find that the dimensionless design parameters t/H, d_0/H, and θ govern the bending behavior of the flap ($d/H - \overline{P}$) and regulation behavior ($\overline{Q} - \overline{P}$) for different levels of pressure.

2.3. Finite element analysis

To validate the theoretical model proposed above, we conduct FEA simulations using the commercial FEA package, COMSOL Multiphysics® (ver. 5.4; Burlington, MA, USA). Specifically, a two-dimensional model consisting of both a solid domain (flap) and a fluid domain (rectangular channel) is established. The solid domain is modeled as an incompressible neo-Hookean material while the fluid domain is modeled as water (which is consistent with the experiments). To account for the interaction between the solid and fluid domain, the fluid–structure interaction (FSI) module in COMSOL is adopted. In the simulation model, a fixed boundary condition is applied to the top end of the flap, which is consistent with the designs (Fig. 2a). The pressure difference ΔP across the entire channel is applied by setting the inlet pressure

of the fluid domain to be ΔP while keeping the outlet pressure of the domain to be zero. Considering that the deformation involved in the simulation can be large, the geometrical nonlinearity is included. A mesh sensitivity analysis is performed to ensure the numerical convergence. The parameters used for modeling are listed in Table S1 in the Supporting Information. After the simulation, both the deformation field (solid domain) and the flow field (fluid domain) can be obtained. To extract the volume flow rate, the integration of the horizontal velocity component along the cross-section of the outlet is performed.

2.4. 3D printing and fabrication

In this paper, we use digit light processing (DLP) 3D printing technique to directly fabricate the fluid channel with the proposed valve design. Figure S2a in the Supporting Information shows the DLP printing setup. It is composed of an ultraviolet (UV) light projector (PRO4500, Wintech, San Marcos, CA, USA) and a linear translation stage (LTS150, Thorlabs, Newton, NJ, USA). The operation of the platform is controlled by a MATLAB script (MathWorks, Natick, MA, USA). In addition, a photocurable liquid resin is prepared by mixing 2-hydroxyethyl acrylate (HEA; Sigma-Aldrich, St. Louis, MO, USA), isodecyl acrylate (IA; Sigma-Aldrich), and Ebecryl 8807 (Allnex, Alpharetta, GA, USA) at a mass ratio of 69.48%: 19.85%: 9.93%. In this material system, HEA and IA are monomers and Ebecryl 8807 is the cross-linker. 0.7 wt% photoinitiator phenylbis (2, 4, 6-trimethylbenzoyl) phosphine oxide (Sigma-Aldrich) and 0.04 wt% photo absorber Sudan I (Sigma-Aldrich) are added into the resin for reaction initiation and improving printing resolution. The mechanical properties of this material are tested on a DMA tester (model Q800, TA Instruments; sample size: ~8 mm × 4 mm × 0.26 mm) and the results can be found in Figure S3 in the Supporting Information.

For the convenience of connecting the valve into the testing system and characterizing the flow rate-pressure responses, a cylindrical inlet and outlet are added at the two ends of the valve channel (Figure S2b, Supporting Information). A full geometry of the valve for testing can be found in the Supporting Information. The length of the main flow channel is 22 mm and the channel height and width are both set to be 1 mm. The dimensions of the flap embedded in the channel vary and depend on the specific design parameters. In addition, a narrow gap between the flap and the sides of the channel is set to be 75 μm so that the flap can move freely without connection to the inner wall at two sides. After determining the geometry of the valve for testing, the final design of the valve is then created in Solidworks (Dassault Systèmes, Vélizy-Villacoublay, France) and transferred to the printing platform for slicing and printing. For the printing, the layer printing time and thickness are set to be 2 s and 100 μm, respectively. For a channel with a length of 30 mm, the printing time is ~30 min. After printing, the sample is fully cleaned with ethanol and transferred to a UV box for overnight post-curing.

2.5. Flow rate measuring system

To experimentally evaluate the performance of the valves, we develop a flow-rate measuring system for characterizing, testing, and analyzing the response of valves for different pressure difference. The system is composed of a pressure regulator (Ultimus V, Nordson, Westlake, OH, USA), a well-sealed container with deionized water, a valve fixture device (printed by PolyJet printer using material Verowhite [37]), a flow meter (SLQ-QT500, Sensirion, Chicago, IL, USA), and a waste-collecting container. In addition, silicone tube segments are used to connect these components. In a typical test, we first set a pressure value P_{test} on the pressure regulator. Then the air on the top of the water container is compressed and its pressure is increased to P_{test}. Under the pressure of P_{test}, the water is delivered into the fluidic path, then flows through the valve and the flow meter, and eventually flows into the waste-collecting container. The flow meter records the flow rate and transfers the data to the computer in real-time.

3. Results and discussion

3.1. Theoretical predictions

In Fig. 3a–f, we report the effects of individual design parameter on the normalized gap d/H and the dimensionless flow rate $\overline{Q}$ as functions of the pressure. In general, excellent agreements between the theoretical model and the FEA simulations are achieved. Fig. 3a shows d/H as a function of $\overline{P}$ for three different dimensionless thicknesses (t/H) with $\theta = 30^\circ$ and $d_0/H = 0.3$. We observe that d/Hmonotonically decreases with increasing $\overline{P}$, which is consistent with our design concept. For a smaller t/H, d/H is more sensitive to the pressure change and decreases more with the same amount increase of $\overline{P}$. This is because that with a higher t/H, a more enhanced flexural stiffness of the flap (proportional to t^3) makes it more difficult for the flap to bend. Furthermore, in Fig. 3a, it is found that a small pressure $\overline{P} \simeq 0.002$ could bend the flap to the bottom wall, or close the channel. Therefore, the flap cannot be designed to be too thin; otherwise, it is too sensitive to pressure and will overreact to the pressure change. Figs. 3b and 3c show d/H as a function of $\overline{P}$ for three different tilt angles (θ) with $d_0/H = 0.3$ and $t/H = 0.3$ and three different initial dimensionless gaps (d_0/H) with $t/H = 0.3$ and $\theta = 30^\circ$, respectively. In Fig. 3b and c, similar results are observed that for all values of θ or d_0/Hunder investigation, d/H decreases as the pressure increases; by either increasing θ or d_0/H, the decrease in d/H versus pressure becomes slower. Although the increase in either θ or d_0/H does not change the bending stiffness of the flap as the increase in t does, the change of θ or d_0/H prominently affects the effective length of the flap l ($l = (H - d_0 - t\cos\theta)/\sin\theta$), which determines the level of the deflection and rotation achieved at the flap end. Therefore, the change of θ or d_0/H also affects d/H. In Fig. 3b and c, we also notice that for a high value of θ (i.e., 40°) or d_0/H (i.e., 0.4), the decrease of d/H from its maximum to its half can span a larger range of pressure than that of low θ or d_0/H. This is desirable for the valve design as it can regulate the flow over a wide range of pressure change.

We next start to analyze the results for the volume flow. In Fig. 3d–f, we plot flow rate curves under the same conditions as those in Fig. 3a–c. In Fig. 3d, we find that in general $\overline{Q}$ first increases with pressure, reaches a peak, and then decreases. This behavior can be understood from the results shown in Fig. 3a. The initial increase in flow is due to the pressure increase, but as the pressure increases, the gap decreases and the flow resistance increases significantly, preventing the further increase of the flow rate. After the peak, the gap decrease dominates and the flow constantly decreases with pressure. For the same amount of pressure, with a higher t/H, $\overline{Q}$ decreases less. The existence of the peak thus indicates the two competing mechanisms due to the increase of the pressure: the increase of the flow rate and the decrease of the gap. In Figs. 3e and 3f, we present the results by varying θ and d_0/H, respectively. For small values of θ or d_0/H, we observe that the behavior of $\overline{Q}$ is similar to that observed in Fig. 3d. However, with increasing θ or d_0/H, the peak becomes less sharp, especially for $\theta = 40^\circ$ or $d_0/H = 4$, in which the flow rate changes negligibly over a wide range of pressure. Note that this behavior corresponds to the situation for high values of θ or d_0/H in Fig. 3b and c where the gap decreases slowly as pressure changes.

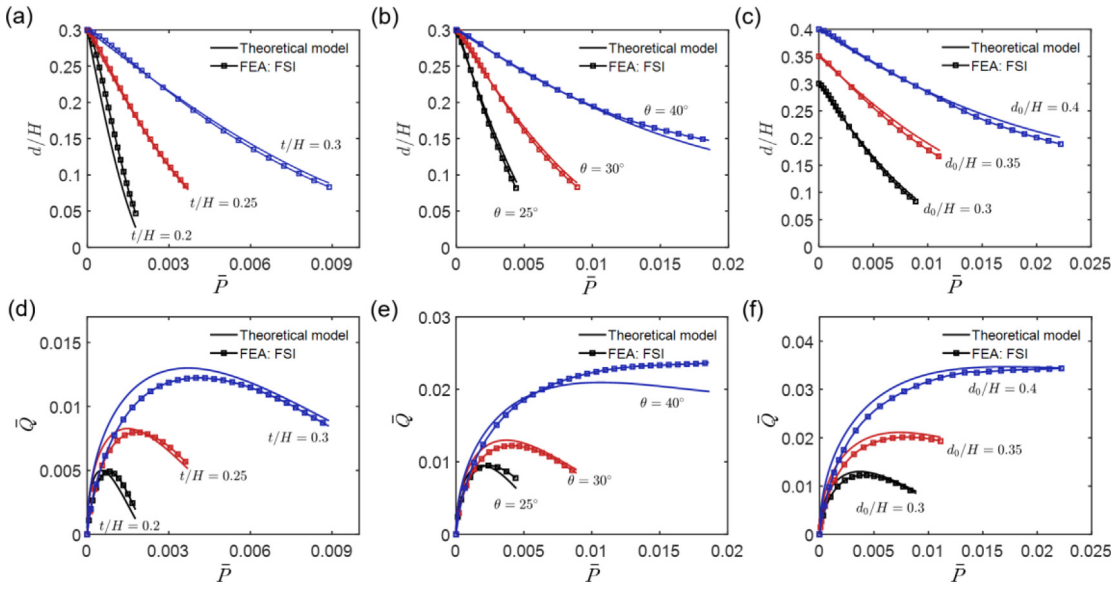

Fig. 3. Investigation of the effects of the design parameters (d_0/H, t/H, θ) on the dimensionless gap-pressure relation ($d/H - \bar{P}$) and flow rate-pressure relation ($\bar{Q} - \bar{P}$) using both the theoretical and finite-element models. Solid lines represent the theoretical results and dotted lines represent the FEA results. (a) d/H as a function of $\bar{P}$ for three different dimensionless thicknesses (t/H) with $\theta = 30°$ and $d_0/H = 0.3$. (b) d/H as a function of $\bar{P}$ for three different tilt angles (θ) with $d_0/H = 0.3$ and $t/H = 0.3$. (c) d/H as a function of $\bar{P}$ for three different initial dimensionless gaps (d_0/H) with $t/H = 0.3$ and $\theta = 30°$. (d) $\bar{Q}$ as a function of $\bar{P}$ for three values of t/H with $\theta = 30°$ and $d_0/H = 0.3$. (e) $\bar{Q}$ as a function of $\bar{P}$ for three values of θ with $d_0/H = 0.3$ and $t/H = 0.3$. (f) $\bar{Q}$ as a function of $\bar{P}$ for three values of d_0/H with $t/H = 0.3$ and $\theta = 30°$.

The above analysis indicates that the regulatory behavior of the channel based on our design scheme is highly tunable; moreover, with the appropriate design parameters, the flow can be regulated and be stable over a wide range of pressure, which is the desired property of a valve for maintaining a constant flow during pressure fluctuations.

3.2. FEA Results

Fig. 3a–f also show that the FEA simulation results agree well with the theoretical results. Moreover, using the FEA simulations, we can understand the deformation of the flap and the flow field involved in our design. In Fig. 4, we present the FEA results for the displacement field, flow field, and pressure distribution for a fluid channel with $t/H = 0.3$, $\theta = 30°$, and $d_0/H = 0.365$. Fig. 4a shows the results of y-displacement distribution of the flap subjected to two different pressure values (7 kPa for the left; 37.5 kPa for the right). Fig. 4a also shows the streamline distribution around the flap demonstrating the variation of the flow field for different flap configuration. Fig. 4b shows the velocity distribution of the fluid (top panel) and the pressure distribution (bottom panel) when the channel is subjected to a pressure difference of 37.5 kPa. On the left of the flap within the channel, the magnitude of the horizontal velocity component of the fluid is ∼2 mm/s, while it is ∼9 mm/s for the fluid on the right of the flap. In addition, the height of the velocity trace along the y-axis direction in the fluid area on the right of the flap is very close to the gap. For the pressure distribution, on the left of the flap, the pressure is a constant value of 37.5 kPa while on the right of the flap, the value is very close to 0 kPa. The pressure drop mainly occur in the area surrounding the flap.

Fig. 4c shows the distribution of velocity V_x at the cross-section A (marked in Fig. 4b) under a series of pressure loadings. The shape of each curve is very close to a parabola. The fluid viscosity leads to the gradient distribution of V_x along the y-axis direction where the velocity value is higher at the center than that in two sides. With increasing the pressure difference, the value of V_x increases but the parabolic shape still holds. Fig. 4d shows the velocity distribution at the cross-section B (marked in Fig. 4b). With decreasing y, V_x first holds values close to zero, then starts to increase rapidly after a certain y-coordinate threshold, which is the close to the value of the gap. After the threshold, the curve shape is roughly close to a parabola. We also notice that for high-pressure loadings (> ∼20 kPa), V_x appears negative at the height above the gap, indicating some back flow toward the flap. Based on the simulation results, we find that behind the valve, the liquid starts to flow across the channel again after a distance of ∼four times the channel height. Therefore, the flow regulator cannot be treated as a single element that controls flow, because its effect also depends on the geometry/length of the channel behind the flow regulator.

3.3. Experimental results

We further validate both theoretical and simulation models by conducting experiments on two different samples. They have the same design parameters (1 mm × 1 mm channel, 30° tilt angle, 300 μm initial gap) except for the thickness (250 μm and 300 μm, respectively). Here, the centerline of the flap with a thickness of 300 μm shifts to a higher position so that the initial gaps of these two flaps are the same. Fig. 5a shows the optical images of the two 3D printed channels with the flaps (top panel for the flap with $t = 250\mu$m; bottom panel $t = 300\mu$m). Fig. 5b shows the experimental setup for characterizing the regulation behaviors of these two samples. Following the method described in Section 2.5, we connect the sample into the measuring system and gradually increase the loading pressure P_{test}. For each P_{test}, the water flow rate is recorded. Fig. 5c–d shows the experimental results. In Fig. 5c, we observe that below a threshold of ∼10 kPa, the flow rate increases as the pressure increases. However, with further increasing pressure, the flow rate starts to decrease. This flow behavior is consistent with the discussions in Section 3.1 and is well captured by the theoretical model and the FEA simulation. For the thicker flap with enhanced flexural stiffness (Fig. 5d), the pressure at the peak flow rate shifts to a higher value (∼15 kPa). In addition, the flow rate also increases compared with that in Fig. 5c for the same amount of pressure.

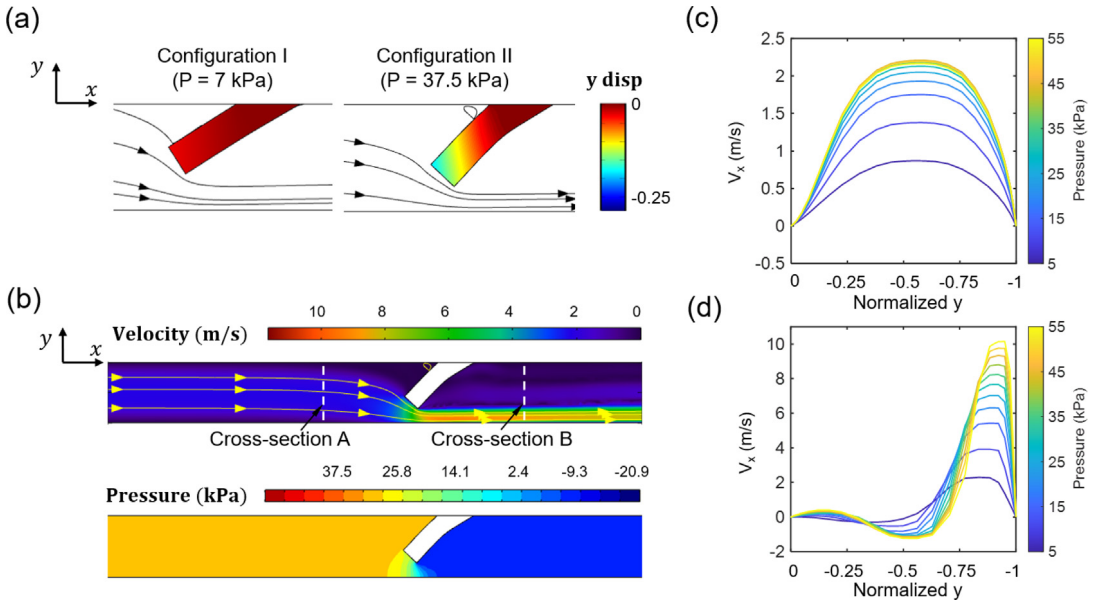

Fig. 4. Numerical results of the displacement field, flow field, and pressure distribution for a fluidic channel with the flap designed to be $t/H = 0.3$, $\theta = 30°$, and $d_0/H = 0.365$. (a) The flap's deformed configuration for two pressure conditions (7 kPa and 37.5 kPa). The colormap in the domain of the flap shows the distribution of y-displacement. Black lines with arrowheads represent streamlines of the fluid. (b) The flow field within the channel for a pressure difference of 37.5 kPa. The top panel shows the velocity field distribution in the fluid domain with yellow lines representing streamlines. The bottom panel shows the pressure distribution in the fluid domain. (c–d) The horizontal velocity component along the cross-section A and B (marked in Fig. 4b) as a function of vertical position for a series of loading pressure values ranging from 5 kPa to 55 kPa.. (For interpretation of the references to color in this figure legend, the reader is referred to the web version of this article.)

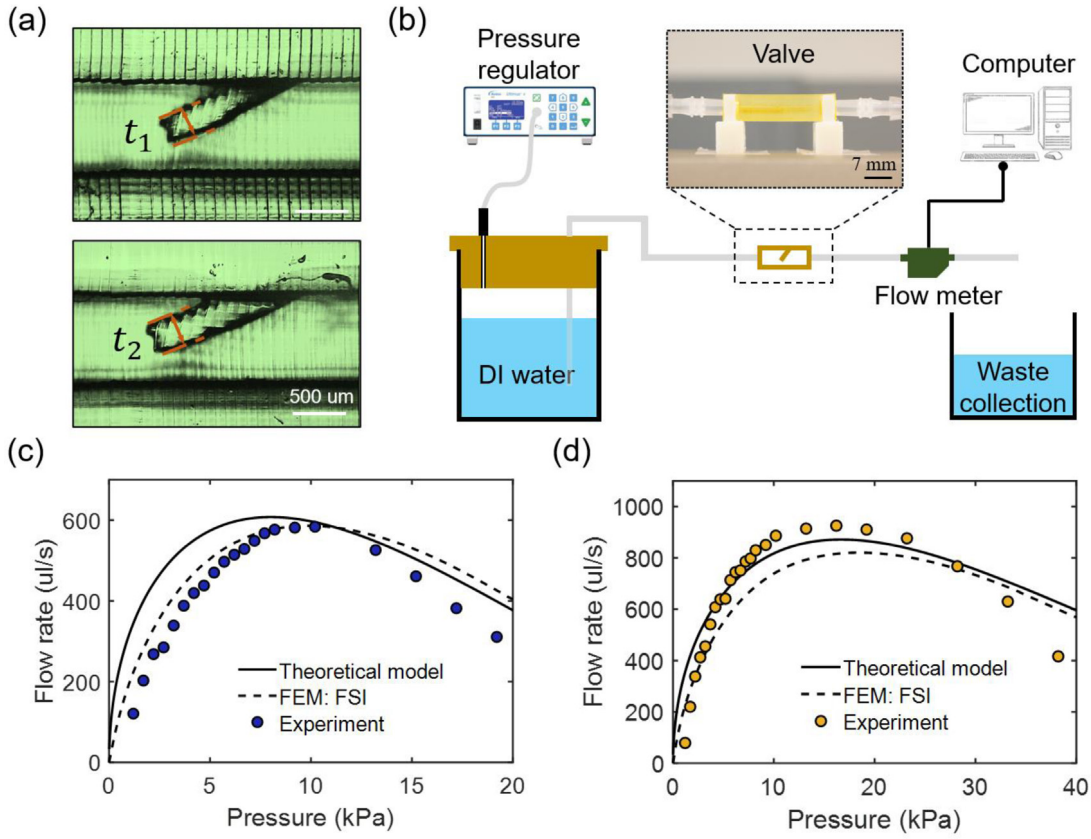

Fig. 5. Experimental characterizations of two valves with different flap thickness. (a) Optical microscopic images showing the cross-section of the printed valves (top panel for the flap with $t = 250$ μm; bottom panel $t = 300$ μm). (b) Schematic graph of the experimental setup for measuring the flow rate under different pressures. The image in the middle of this graph shows a valve sample being in testing. (c–d) Flow rate as a function of pressure for the valve with a flap thickness of 250 μm and 300 μm, respectively. Solid line represents results from the theoretical model. Dashed line represents results from FEA. Dots represent experimental results.

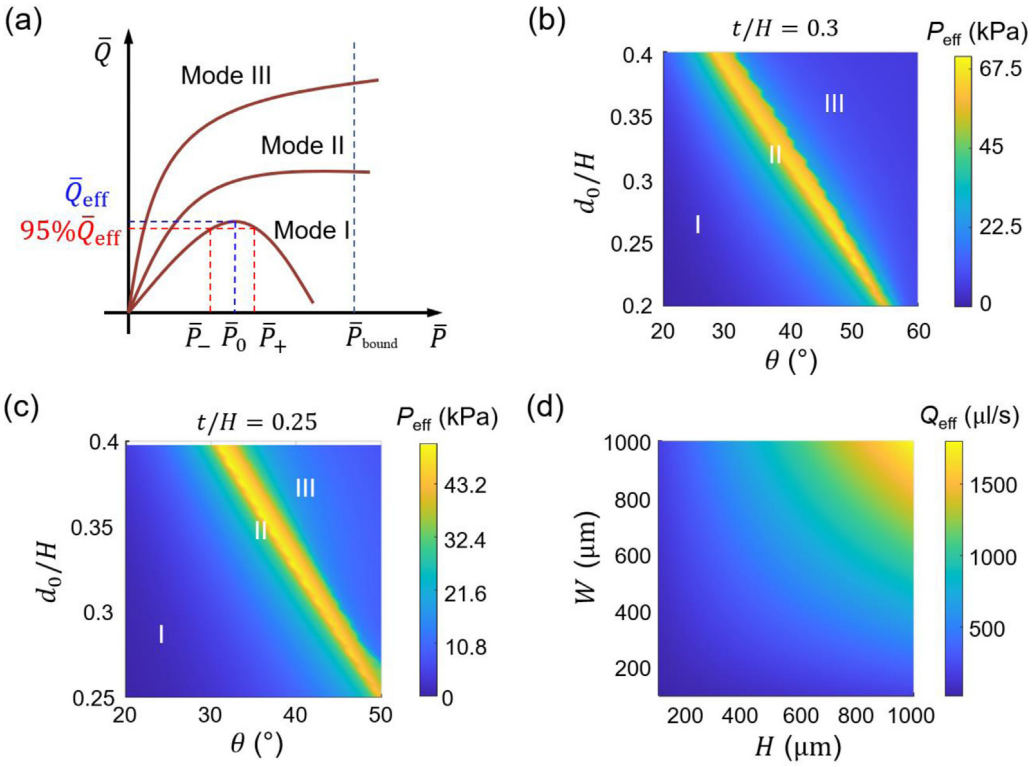

Fig. 6. Design guidelines for valves with different flow rate-pressure responses. (a) Schematic graph of the three typical flow rate-pressure responses that we refer to as mode I, II, and III, respectively. For all the three modes, the maximum $\bar{Q}$ and its 95% are denoted as $\bar{Q}_{eff}$ and 95%$\bar{Q}_{eff}$, respectively. Two $\bar{P}$ values at which $\bar{Q}$ satisfies $\bar{Q} = 95\%\bar{Q}_{eff}$ are denoted as $\bar{P}_+$ and $\bar{P}_-$, respectively. The pressure at which the flow rate $\bar{Q} = \bar{Q}_{eff}$ is defined as $\bar{P}_0$. (b) Design space (θ, d_0/H) for each mode with the relative thickness t/H fixed to be 0.3. Colormap represents the effective pressure range P_{eff}, which is defined via $P_{eff} = E\left(\bar{P}_+ - \bar{P}_-\right)$. (c) Design space ($\theta$, d_0/H) for each mode with the relative thickness t/H fixed to be 0.25. Colormap represents the effective pressure range. (d) Efficient flow rate versus height and width of the valve channel for the design point $t/H = 0.3$, $\theta = 40°$, and $d_0/H = 0.3$. The effective flow rate Q_{eff} is obtained via $Q_{eff} = \bar{Q}_{eff} HW\sqrt{E/\rho}$.. (For interpretation of the references to color in this figure legend, the reader is referred to the web version of this article.)

3.4. Design guidelines for valves with different regulation behaviors

The theoretical model in Section 2.1 can be used for rapidly optimizing the flap geometry for achieving channels with tailored regulation behavior. For the sake of simplicity, we fix $t/H$to be several specific values while changing θ and d_0/H to obtain the desired design space. Through the theoretical model, we find that there are three types of flow rate-pressure responses, which we refer to as mode I, II, and III, respectively. Fig. 6a shows schematically the $\bar{Q} - \bar{P}$ curves of these three modes. Note that these modes are also observed in Fig. 3d–f. For mode I, the flow rate first increases and then decreases after a certain threshold of pressure. For mode II, the flow rate first increases and then nearly stabilizes for a certain range of pressure. For mode III, the flow rate always increases with pressure. To assist the design, we further define some performance parameters. First of all, we can select a pressure upper bound $\bar{P}_{bound}$ to define the working pressure range ($0 \sim \bar{P}_{bound}$) for the regulator. Next, we denote the peak volume flow rate $\bar{Q}$ as $\bar{Q}_{eff}$ and the two $\bar{P}$ values at which $\bar{Q}$ satisfies $\bar{Q} = 95\%\bar{Q}_{eff}$ as $\bar{P}_+$ and $\bar{P}_-$, respectively. The pressure at which the flow rate $\bar{Q} = \bar{Q}_{eff}$ is defined as $\bar{P}_0$. With these parameters, the three modes can be mathematically distinguished as

$$\begin{aligned} &\bar{P}_+ \le \bar{P}_{bound} && \text{, mode I} \\ &\bar{P}_0 < \bar{P}_{bound} < \bar{P}_+ && \text{, mode II} \\ &\bar{P}_{bound} \le \bar{P}_0 && \text{, mode III.} \end{aligned} \tag{15}$$

Based on the above classification, the effective pressure range for each mode can be defined as $P_{eff} = E\left(\bar{P}_+ - \bar{P}_-\right)$ for mode I, $P_{eff} = E\left(\bar{P}_{bound} - \bar{P}_-\right)$ for mode II, and $P_{eff} = E\left(\bar{P}_{bound} - \bar{P}_-\right)$ for mode III, respectively. And the effective flow rate is obtained via $Q_{eff} = \bar{Q}_{eff} HW\sqrt{E/\rho}$. The t/H value of 0.3 and 0.25 are taken here as two examples to illustrate the design process. In Fig. 6b, for the design space covering $\theta \in [20°, 60°]$ and $d_0/H \in [0.2, 0.4]$, mode I is mainly located in the lower triangular area, mode III is located in the upper triangular area, and mode II is located in the area near the diagonal. In order to design flow regulators that can maintain a constant flow rate over a wide range of pressure, we can choose the design points from the mode II area. Likewise, if we need a regulator that is able to shut off the flow during overpressure, we can choose the design points from the mode I area. For other, similar design graphs can be obtained as Fig. 6b. For example, Fig. 6c shows the results for $t/H = 0.25$. As the relative thickness of 0.25 is smaller than 0.3, the flap of the valve in this case is relatively more flexible than that in Fig. 6b. Therefore, compared with Fig. 6b, for achieving the same efficient pressure range, a design point with either a higher θ or d_0/H is needed. After determination of the design point, we can then choose the proper cross-section dimension of the valve channel to obtain the desired flow rate that can be maintained over a certain range of pressure. Fig. 6d shows the different flow rate range versus the height and width of the channel for a design point with $t/H = 0.3$, $\theta = 40°$, and $d_0/H = 0.3$, which is located in the design space in Fig. 6b. By properly reducing the cross-section of the channel, the flow rate can be widely tunable, indicating the current method can be used to design valves that maintain different constant flow rates over a wide range of pressure.

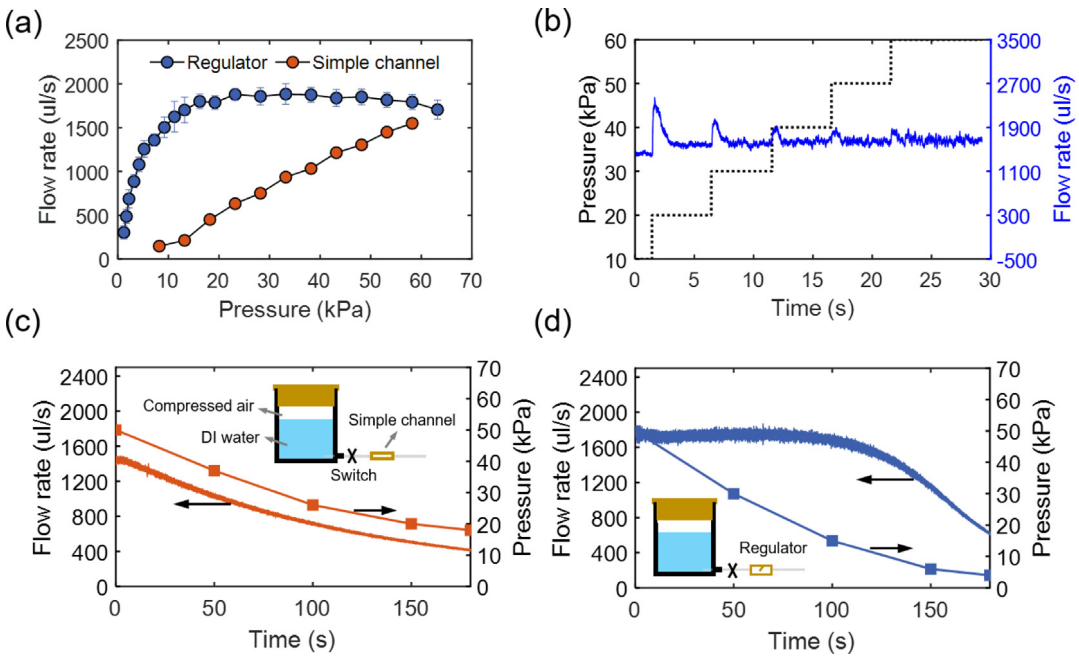

Fig. 7. Evaluation of a flow regulator for stabilizing the flow rate under varying pressure. (a) Flow rate as a function of pressure for the regulator (with a tilt angle of 40°, a thickness of 300 μm, and an initial gap of 300μm) and the simple channel (cross-section: 500 ×500 μm) without internal flaps. (b) Pressure loading (black line) and flow rate response (blue line) as a function of time. (c) Flow rate (solid line) and pressure of the air inside the container (dotted line) as a function of time for the regulator. (d) Flow rate (solid line) and pressure of the air inside the container (dotted line) as a function of time for the simple channel. (For interpretation of the references to color in this figure legend, the reader is referred to the web version of this article.)

3.5. A flow regulator for stabilizing the flow rate under varying pressure

In this section, we employ the above design guideline to develop a passive flow regulator that can maintain a constant flow rate over a wide range of pressure and evaluate its performance. In order to do this, we firstly select the proper design parameters from Fig. 6. Our goal here is to ensure the flow can be stabilized by the regulator despite the pressure changes. Therefore, we can choose the design point with a relatively large efficient pressure range from the mode II area in Fig. 6b. Here, we choose the design point which satisfies $t/H = 0.3$, $\theta = 40°$, and $d_0/H = 0.3$. We next determine both the height and width of the regulator to be 1 mm. Under these design parameters, we then fabricate the regulator according to the method described in Section 2.4. To evaluate the performance of the valve under this design, we firstly measure the flow behavior of the valve using the setup shown in Fig. 5b. Fig. 7a shows the flow rate of the regulator obtained at different loading pressure levels (blue dotted line). It is found that the flow rate first increases with the increasing pressure; after ∼20 kPa, the flow rate shows no noticeable change in the range of 20–60 kPa, indicating that the regulator can work in a system where the pressure fluctuations are within this range. The constant flow rate is found to be 1850.2 ± 106.9 ul/s with a deviation (5.78%) smaller than 6%. To more clearly show the stability of the flow rate within this range, we next input a series of changing pressure to drive the flow and observe the flow rate response. As an example, we establish a pressure loading process in which the pressure increases step-wisely from 10 kPa to 60 kPa with the step set as 10 kPa. Fig. 7b shows the pressure loading versus time (black line). At the beginning, the initial pressure value is 10 kPa and it lasts for a period of ∼1.3 s. Subsequently, the pressure is increased by 10 kPa in every 5 s until the pressure reaches 60 kPa. During this process, the water is continuously flowing through the regulator and the flow rate is measured within this period. Fig. 7b presents the results of the flow rate versus time (blue line). We find that despite the pressure changes, the flow rate within this period is overall steady and nearly not changing. Specifically, for the first ∼1.3 s, the flow rate is ∼1500 μl/s, subsequently, there is an overshoot in the flow rate after the first step increase in pressure (from 10 kPa to 20 kPa). The overshoot then disappears in the next few seconds and the flow rate recovers to a steady-state value before the next pressure increase. Small overshoots are also observed in the next few step-increases of pressure but the steady flow rate value after each overshoot is nearly identical. It is understandable that the overshoots observed here are caused by the large pressure change in the step pressure input, which is consistent to the overshoot phenomenon frequently observed in the output of low-pass filters for a step signal input [38,39].

To demonstrate the capabilities of the above flow regulator in real applications, we next conceive an application scenario. In the scenario, we consider a container of water flowing out through a channel connected to its bottom (the schematic graph in Figs. 7c and d). On the top of the water, there is an amount of compressed air. At the initial moment, the pressure of the compressed air is set to be 50 kPa. When the switch is open, the water starts to flow out of the container due to the air pressure. As the top surface of the water drops, the pressure of the air also drops. Without a regulator, the flow rate will continuously decrease. Our goal here is to maintain a constant flow rate as the water drains using the regulator we create. For performance comparison, we also fabricate a simple long and narrow channel (with a cross-section of 500 ×500 μm) without any internal flaps as a reference. Fig. 7a shows the flow behavior as a function of the pressure for this reference channel (orange dotted line). It indicates that the flow rate monotonically increases as the pressure increases, showing no regulatory effects on the flow rate. When connecting this simple channel into the setup, as expected, the flow rate continuously decreases, as shown in Fig. 7c. By contrast, when connecting the flow regulator into the setup, the flow rate is almost constant in the first 100 s, as shown in Fig. 7d. After ∼100 s, the flow rate begins to decrease because the pressure of the compressed air at this moment is below 20 kPa (dotted line

in Fig. 7d). Through this comparison, we conclude that the flow regulator used here is efficient for stabilizing the flow rate over a wide range of pressure.

3.6. Discussion

Previous researches have shown that the high-throughput flow rate control is very useful for applications such as the continuous concentration of trace blood cells from large-volume biofluids [34]. It should be mentioned that although a large flow rate can possibly be exploited for high-throughput flow rate control in the microfluidic environment [18], the flow rate scale ($\sim$1000 μl/s) we experimentally demonstrate in this work is relatively larger than other researches ($\sim$1-70 μl/s) [23,32]. However, the geometry of the valve based on our design can be properly scaled to provide any desired flow rate and most of the discussions in this work should still be valid. For example, by decreasing both the height and width of the cross-section of the regulator demonstrated in Section 3.5 from 1 mm to 200 μm while changing the parameters of the flap to be the corresponded scaled values (that is, the tilt angle holds for 40° while the thickness becomes 60 μm, and the initial gap becomes 60 μm), based on prediction, we can achieve a stable flow rate of $\sim$70 μl/s (Fig. 6d). With the latest advances in using 3D printing techniques to fabricate microfluidic devices down to $\sim$ 20 μm [40–44], it is feasible to manufacture our valves with a finer size to provide smaller flow rates. On the other hand, for applications such as flow-driven soft robotics where a higher flow rate is required, we could accordingly scale up the geometry of the flow regulator to accommodate the application task. For example, by enlarging the channel size and flap at the same scale, the performance of the obtained regulator (nondimensional flow rate-pressure) will keep unchanged while the flow rate will be scaled up. In all, the new structural design and the associated quantitative design tool proposed here can enrich the existing valve designs, providing the possibility to develop a variety of devices for different applications such as portable drug delivery systems.

4. Conclusion

In this work, we present a new design for creating a fluidic channel that can serve as a passive valve to regulate the flow rate under pressure variations. A theoretical analysis is performed to understand the effects of the critical design parameters on the nonlinear flow rate-pressure relations. The model is validated by the FEA simulations and the experiments. We then use the theoretical model to develop a rational design tool for guiding the design of the valve to obtain different flow rate responses and optimized performance. Based on the quantitative design tool and the printing platform, we create a passive valve that can stabilize the flow rate under varying pressure conditions and show good capabilities.

Declaration of competing interest

The authors declare that they have no known competing financial interests or personal relationships that could have appeared to influence the work reported in this paper.

Acknowledgments

Q. Z. greatly acknowledges the support from China Scholarship Council (Grant No. 201806010291). R.Z. acknowledges the support from Juvenile Diabetes Research Foundation, USA (JDRF, 2-SRA-2019-853-S-B).

Appendix A. Supplementary data

Supplementary material related to this article can be found online at https://doi.org/10.1016/j.eml.2020.100824.

References

[1] C.J. Bettinger, et al., Silk fibroin microfluidic devices, Adv. Mater. 19 (5) (2007) 2847–2850.
[2] J.J.T. Wang, Electrochemical detection for microscale analytical systems: a review, 56 (2), 2002, pp. 223–231.
[3] J.C. McDonald, et al., Fabrication of microfluidic systems in poly (dimethylsiloxane), 21 (1), 2000, pp. 27–40.
[4] J. Wegner, S. Ceylan, A. Kirschning, Ten key issues in modern flow chemistry, Chem. Commun. (Camb.) 47 (16) (2011) 4583–4592.
[5] L. Malet-Sanz, F. Susanne, Continuous flow synthesis. A pharma perspective, J. Med. Chem. 55 (9) (2012) 4062–4098.
[6] B. Ziaie, et al., Hard and soft micromachining for BioMEMS: review of techniques and examples of applications in microfluidics and drug delivery, Adv. Drug Deliv. Rev. 56 (2) (2004) 145–172.
[7] J. Yu, et al., Microneedle-array patches loaded with hypoxia-sensitive vesicles provide fast glucose-responsive insulin delivery, Proc. Natl. Acad. Sci. USA 112 (27) (2015) 8260–8265.
[8] K.M. Bratlie, et al., Materials for diabetes therapeutics, Adv. Healthc. Mater. 1 (3) (2012) 267–284.
[9] J.C. Pickup, B. M, D. Phil, Insulin-pump therapy for type 1 diabetes mellitus, New Engl. J. Med. 366 (2012) 1616–1624.
[10] R. Hovorka, et al., Overnight closed loop insulin delivery (artificial pancreas) in adults with type 1 diabetes: crossover randomised controlled studies, BMJ 342 (2011) d1855.
[11] T.T. Goodnow, M.L. Blomquist, J.G. Johnson, Glucose measuring module and insulin pump combination, 2013, Google Patents.
[12] J.G. Smits, Piezoelectric micropump with three valves working peristaltically, Sensors Actuators A 21 (1–3) (1990) 203–206.
[13] A. Ullmann, The piezoelectric valve-less pump—performance enhancement analysis, Sensors Actuators A 69 (1) (1998) 97–105.
[14] Y. Bozhi, L. Qiao, A latchable phase-change microvalve with integrated heaters, J. Microelectromech. Syst. 18 (4) (2009) 860–867.
[15] W. Zhang, et al., PMMA/PDMS valves and pumps for disposable microfluidics, Lab Chip 9 (21) (2009) 3088–3094.
[16] H. Kim, J. Kim, A microfluidic-based dynamic microarray system with single-layer pneumatic valves for immobilization and selective retrieval of single microbeads, Microfluid. Nanofluid. 16 (4) (2013) 623–633.
[17] A.R. Abate, D.A. Weitz, Single-layer membrane valves for elastomeric microfluidic devices, Appl. Phys. Lett. 92 (24) (2008).
[18] A.R. Abate, J.J. Agresti, D.A. Weitz, Microfluidic sorting with high-speed single-layer membrane valves, Appl. Phys. Lett. 96 (20) (2010).
[19] J. Xie, J. Shih, Y.-C. Tai, Integrated surface-micromachined mass flow controller, in: The Sixteenth Annual International Conference on Micro Electro Mechanical Systems, IEEE, Kyoto, Japan, 2003, pp. 20–23.
[20] S.R. Sershen, et al., Independent optical control of microfluidic valves formed from optomechanically responsive nanocomposite hydrogels, Adv. Mater. 17 (11) (2005) 1366–1368.
[21] J. Casals-Terré, et al., Design and characterization of a magnetic digital flow regulator, Sensors Actuators A 162 (1) (2010) 107–115.
[22] T. Hoare, et al., Magnetically triggered nanocomposite membranes: a versatile platform for triggered drug release, Nano Lett. 11 (3) (2011) 1395–1400.
[23] I. Doh, Y.H. Cho, Passive flow-rate regulators using pressure-dependent autonomous deflection of parallel membrane valves, Lab Chip 9 (14) (2009) 2070–2075.
[24] B. Yang, Q. Lin, Planar micro-check valves exploiting large polymer compliance, Sensors Actuators A 134 (1) (2007) 186–193.
[25] E.P. Kartalov, et al., Microfluidic vias enable nested bioarrays and autoregulatory devices in Newtonian fluids, Proc. Natl. Acad. Sci. 103 (33) (2006) 12280–12284.
[26] H.J. Chang, W. Ye, E.P. Kartalov, Quantitative modeling of the behaviour of microfluidic autoregulatory devices, Lab Chip 12 (10) (2012) 1890–1896.
[27] P. Cousseau, et al., Improved micro-flow regulator for drug delivery systems, in: Proceeding of the 14th IEEE International Conference on Micro Electro Mechanical Systems, MEMS 2001, IEEE, Interlaken, Switzerland, 2001, pp. 527–530.
[28] A. Groisman, M. Enzelberger, S.R. Quake, Microfluidic memory and control devices, Science 300 (5621) (2003) 955–958.
[29] M.S. Sacks, W.D. Merryman, D.E. Schmidt, On the biomechanics of heart valve function, J. Biomech. 42 (12) (2009) 1804–1824.
[30] B. Yang, Q. Lin, A planar compliance-based self-adaptive microfluidvariable resistor, J. Microelectromech. Syst. 16 (2) (2007) 411–419.

[31] X. Zhang, et al., Passive flow regulator for precise high-throughput flow rate control in microfluidic environments, RSC Adv. 6 (38) (2016) 31639–31646.
[32] X. Zhang, et al., A passive flow regulator with low threshold pressure for high-throughput inertial isolation of microbeads, Lab Chip 15 (17) (2015) 3473–3480.
[33] X. Zhang, et al., A microfluidic gas damper for stabilizing gas pressure in portable microfluidic systems, Biomicrofluidics 10 (5) (2016) 054123.
[34] N. Xiang, et al., Flow stabilizer on a syringe tip for hand-powered microfluidic sample injection, Lab Chip 19 (2) (2019) 214–222.
[35] J.M. Gere, S.P. Timoshenko, Mechanics of Materials, fourth ed., PWS Pub. Co., Boston, 1997.
[36] B.R. Munson, et al., Fluid Mechanics, Wiley Singapore, 2013.
[37] Z. Ding, et al., Direct 4d printing via active composite materials, Sci. Adv. 3 (2017) e1602890.
[38] Y.-S. Lu, C.-M. Cheng, C.-H. Cheng, Non-overshooting PI control of variable-speed motor drives with sliding perturbation observers, Mechatronics 15 (9) (2005) 1143–1158.
[39] A. Ali, S. Majhi, PI/PID controller design based on IMC and percentage overshoot specification to controller setpoint change, ISA Trans. 48 (1) (2009) 10–15.
[40] C.I. Rogers, et al., 3D printed microfluidic devices with integrated valves, Biomicrofluidics 9 (1) (2015) 016501.
[41] T. Monaghan, et al., Customisable 3D printed microfluidics for integrated analysis and optimisation, Lab Chip 16 (17) (2016) 3362–3373.
[42] M.J. Beauchamp, G.P. Nordin, A.T. Woolley, Moving from millifluidic to truly microfluidic sub-100-mum cross-section 3D printed devices, Anal. Bioanal. Chem. 409 (18) (2017) 4311–4319.
[43] H. Gong, et al., Custom 3D printer and resin for 18 mum × 20 mum microfluidic flow channels, Lab Chip 17 (17) (2017) 2899–2909.
[44] G. Weisgrab, A. Ovsianikov, P.F. Costa, Functional 3D printing for microfluidic chips, Adv. Mater. Technol. 4 (10) (2019) 1900275.